Radiation hydrodynamics of triggered star formation: the effect of the diffuse radiation field

Thomas J. Haworth⋆ and Tim J. Harries
School of Physics, University of Exeter, Stocker Road, Exeter EX4 4QL

ABSTRACT
We investigate the effect of including diffuse field radiation when modelling the radiatively driven implosion of a Bonnor-Ebert sphere (BES). Radiation-hydrodynamical calculations are performed by using operator splitting to combine Monte Carlo photoionization with grid-based Eulerian hydrodynamics that includes self-gravity. It is found that the diffuse field has a significant effect on the nature of radiatively driven collapse which is strongly coupled to the strength of the driving shock that is established before impacting the BES. This can result in either slower or more rapid star formation than expected using the on-the-spot approximation depending on the distance of the BES from the source object. As well as directly compressing the BES, stronger shocks increase the thickness and density in the shell of accumulated material, which leads to short, strong, photo-evaporative ejections that reinforce the compression whenever it slows. This happens particularly effectively when the diffuse field is included as rocket motion is induced over a larger area of the shell surface. The formation and evolution of 'elephant trunks' via instability is also found to vary significantly when the diffuse field is included. Since the perturbations that seed instabilities are smeared out elephant trunks form less readily and, once formed, are exposed to enhanced thermal compression.

Key words: stars: formation – ISM: HII regions – ISM: kinematics and dynamics – hydrodynamics – radiative transfer – methods: numerical

1 INTRODUCTION

The majority of stars form in clusters, situated in molecular clouds that range in size from less than a single parsec to several hundred parsecs (Lada & Lada 2003). In order for star formation to occur, gravitational collapse of material has to overcome internal thermal pressure, supersonic material motions (turbulence) and magnetic fields (see e.g. Preibisch & Zinnecker 2007; Hartmann 2009). The presence of OB stars in these systems has a dramatic impact on the surrounding material (and therefore star formation), as they emit large amounts of high energy radiation that photoionizes gas and gives rise to propagating ionization and shock fronts (Elmegreen 2011). They also inject mechanical energy into the surroundings in the form of high-speed stellar winds and, eventually, supernova explosions. The net impact of radiative feedback from massive stars on star formation efficiency in a molecular cloud is currently unclear, though a number of individual processes that either inhibit or induce further star formation has been identified.

The two main radiative feedback mechanisms that inhibit star formation are the dispersal of material that might otherwise move towards the centre of the molecular clouds' gravitational potential (e.g. Herbig 1962) and the possibility of driving and maintaining turbulence that supports against collapse (e.g. Peters et al. 2008; Gritschneder et al. 2009).

The two primary established mechanisms for the induction of star formation are consequences of the expanding ionization and shock fronts about a massive star. The first is 'collect and collapse' (Elmegreen & Lada 1977; Elmegreen et al. 1995; Dale et al. 2007) in which material that is accumulated by the expanding ionization front of an HII-region becomes locally gravitationally unstable, fragmenting and collapsing to form stars. This mechanism is supported observationally by, for example, the identification of massive fragments located in a dust ring surrounding the HII region RCW 79 by Zavagno et al. (2006).

The second mechanism is radiatively driven implosion (RDI), (Bertoldi 1989) in which radiatively induced shocks drive into otherwise stable pre-existing density structures and cause them to collapse and form stars. RDI has been

⋆ E-mail: haworth@astro.ex.ac.uk

modelled by various groups, for example Kessel-Deynet & Burkert (2003), Arthur & Hoare (2006), Gritschneder et al. (2009), Henney et al. (2009), Bisbas et al. (2011) and produces objects similar to observed bright rimmed clouds (BRCs) in HII regions (Ogura et al. 2002). The rate at which collapse occurs and the associated star forming efficiency of these RDI models has unsurprisingly been found to be very sensitive to the incoming flux.

A variant of collect and collapse, in which the trigger for fragmentation of an ionization front is one of the many possible hydrodynamic or radiation hydrodynamic instabilities has also been explored (e.g. Vishniac 1983; Garcia-Segura & Franco 1996; Williams 2002; Mizuta et al. 2006). When sufficiently perturbed, faster moving components of the ionization front will funnel material transversely to the direction of I-front propagation, depositing it in the path of slower moving components (Vishniac 1983; Garcia-Segura & Franco 1996). This results in a collection of pillar-like objects with dense tips, much as is observed in e.g. the pillars of creation in the Eagle Nebula or the Dancing Queen's Trunk in NGC7822 (see e.g. Schneps et al. 1980; Reach et al. 2004; Chauhan et al. 2011).

Recently, Gritschneder et al. (2009) and Gritschneder et al. (2010) used the ray-tracing, smooth particle hydrodynamics (SPH) code, iVINE (Gritschneder et al. 2009) to consider the effects of a radiation front impinging upon a turbulent neutral medium. They found that radiation could support turbulence, which would prohibit large-scale star formation by supporting against collapse. They also found that ionizing radiation rapidly penetrated lower density regions, heating them up and compressing the remaining higher density structures. This again resulted in pillars with dense cores at the tips where stars might form. They termed this process 'radiative round-up'.

Each of the aforementioned processes has been the subject of numerical modelling. Due to the intensive computational demand of these models, at least in three dimensions, a number of approximations have necessarily been developed. Ercolano & Gritschneder (2011a) provides an overview and evaluation of some of the main approximations, summarised as follows.

a) Considering a monochromatic radiation field, usually Lyman 13.6eV photons, reduces calculation timescales (as with all of these approximations) compared with polychromatic models. This is because the entire source spectrum does not need to be resolved and a single value can be used for the gas opacity. However, this speed up is at the expense of being able to reliably calculate the resulting ionization and temperature structure of the system and neglects effects due to radiation hardening (though radiation hardening effects can be estimated in monochromatic codes, e.g. Mellema et al. 2006).

b) Use of simplified thermal balance calculations, for example calculating the temperature as a simple function of the ionization fraction. This is more straightforward to implement and results in faster calculations than solving the thermal balance by comparing heating and cooling rates.

c) Assuming that the system is in photoionization equilibrium. This is valid where recombination timescales are shorter than the dynamical timescales of the gas.

d) The 'on the spot' (OTS) approximation. Under this scheme diffuse field photons, those generated in recombination events, are not treated. This is justified in regimes where diffuse field photons will not propagate very far and therefore not modify the global ionization structure significantly. It is however, questionable in regions of low or rapidly varying density. Because diffuse field photons are emitted isotropically, it is possible that shadowed regions will not be exposed to a realistic amount of ionizing radiation when modelled under the OTS approximation.

It is not yet clear what impact these approximations have on both the inhibiting and inducing mechanisms described above. In an effort to understand the effect of the diffuse field, Ercolano & Gritschneder (2011a) compared snapshots from the radiative round-up models run by iVINE, with full radiative transfer calculations using the Monte-Carlo radiative transfer code MOCASSIN (Ercolano et al. 2003) and noted significant differences between the ionization and temperature structures calculated by the two codes. Ercolano & Gritschneder (2011b) subsequently attempted to account for the thermal effects of the diffuse field in iVINE by identifying shadowed regions and assigning them a parameterised temperature as a function of density based on comparisons of iVINE and MOCASSIN snapshots. Using this shadowing scheme a significant effect on the resulting pillar structures was observed. Far fewer pillars were formed and those that remained were narrower, denser and often cut off from the parent molecular cloud due to their parameterised increased exposure to ionizing radiation from the diffuse field. This leads to earlier triggering of star formation and reduces the efficiency of radiation driven turbulence. This shadowing scheme is not without drawbacks, being susceptible to erroneous heating of true shadowed regions. The spread in temperatures at a given density calculated by MOCASSIN also results in quoted typical errors in parameterized temperature of approximately 50%. It is certainly clear from this work that a more comprehensive knowledge of the effects of the diffuse field would be valuable. It will be necessary to establish just how different the result of a radiation hydrodynamics calculation can be when incorporating the diffuse field directly, to validate or reassess the use of simplified radiation handling in radiative feedback simulations.

In this work we use the radiation hydrodynamics code TORUS (Harries 2000; Kurosawa et al. 2004; Harries et al. 2004; Acreman et al. 2010; Harries 2011) to investigate the effects on radiatively driven implosion of a more sophisticated treatment of the diffuse field than previously applied in a radiation hydrodynamics calculation. Specifically, we will systematically deduce the relative effects of using a monochromatic OTS, polychromatic OTS and polychromatic-diffuse radiation field on the overall nature of collapse.

2   NUMERICAL METHOD

2.1   Hydrodynamics

We use a flux conserving, finite volume hydrodynamics algorithm. It is total variation diminishing (TVD) and makes use of the Superbee flux limiter (Roe 1985). We also incorporate a Rhie-Chow interpolation scheme (Rhie & Chow 1983) to avoid 'checkerboard' effects that may otherwise appear in cell-centred grid-based hydrodynamics codes.

2.2   Self-Gravity

In order to include self-gravity we solve Poisson's equation

$$\nabla^2 \phi = 4\pi G \rho \tag{1}$$

where ϕ and ρ are the gravitational potential and matter density respectively.

We use a multigrid method employing Gauss-Seidel sweeps with successive over-relaxation to solve a linearized version of equation 1 over the grid. We impose Dirichlet boundary conditions with the potential at the boundary set to a multipole expansion of the matter interior to the boundary (including terms up to the quadrupole). The gravitational potential is subsequently included as a source term in the hydrodynamical equations.

2.3   Photoionization

Photoionization calculations are performed here using an iterative Monte Carlo photon packet propagating routine, similar to that of Ercolano et al. (2003) and Wood et al. (2004) which in turn are based on the methods presented by Lucy (1999).

Photon packets are collections of photons for which the total energy ϵ remains constant, but the number of photons contained varies for different frequencies ν. These are initiated at stars in the model, with frequencies selected randomly based on the emission spectrum of the star. The constant energy value ϵ for each photon packet is simply the total energy emitted by stars (luminosity L) during the duration Δt of the iteration divided by the total number of photon packets N:

$$\epsilon = \frac{L\Delta t}{N} \tag{2}$$

Once initiated, a photon packet will propagate for a path length p determined by a randomly selected optical depth as detailed in Harries & Howarth (1997). If the photon packet fails to escape a cell after travelling p then its propagation ceases and an absorption event occurs. Under the OTS approximation, once a photon packet is absorbed it is ignored, being assumed to either have been re-emitted with a frequency lower than that required for photoionization, or provide negligible further contribution to the ionization structure by causing further photoionization on only small scales. Using the principle of detailed balance, after an absorption event a new photon packet is immediately emitted from the same location with a new isotropically random direction and a new random frequency based on the temperature dependent emission spectrum. This process repeats until the photon packet escapes the grid, or its propagation time matches the current simulation time. For each cell in

the grid the sum of the paths l that photon packets traverse is recorded.

Note that the energy density dU of a radiation field is given by

$$dU = \frac{4\pi J_\nu}{c} d\nu \tag{3}$$

where c is the speed of light. A photon packet having a path l in a particular cell contributes an energy $\epsilon(l/c)/\Delta t$ to the time-averaged energy density of that cell. Thus by summing over all paths l the energy density of a given cell (volume V) can be determined, and by equation 3 the mean intensity may be estimated:

$$\frac{4\pi J_\nu}{c} d\nu = \frac{\epsilon}{c\Delta t} \frac{1}{V} \sum_{d\nu} l. \tag{4}$$

This is then used to obtain ionization fractions by solving the ionization balance equation (Osterbrock 1989)

$$\frac{n(X^{i+1})}{n(X^i)} = \frac{1}{\alpha(X^i)n_e} \int_{\nu_1}^{\infty} \frac{4\pi J_\nu a_\nu(X^i) d\nu}{h\nu} \tag{5}$$

where $n(X^i)$, $\alpha(X^i)$, $a_\nu(X^i)$, n_e and ν_1 are the number density of the ith ionization state of species X, recombination coefficient, absorption cross section, electron number density and the threshold frequency for ionization of species X^i respectively. In terms of Monte Carlo estimators (equation 4), equation 5 is given by

$$\frac{n(X^{i+1})}{n(X^i)} = \frac{\epsilon}{\Delta t V \alpha(X^i)n_e} \sum \frac{l a_\nu(X^i)}{h\nu} \tag{6}$$

This approach has the advantage that photon packets contribute to the estimate of the radiation field without having to undergo absorption events, thus even very optically thin regions are properly sampled.

TORUS performs photoionization calculations that incorporate a range of atomic species and in which thermal balance in each cell is calculated by iterating on the temperature until the heating and cooling rates match.

For the radiation hydrodynamics models in this paper a simplified thermal balance calculation is used and the only species considered are atomic and ionized hydrogen. This is to allow for comparison with previous works that use these schemes such as Gritschneder et al. (2009) and Bisbas et al. (2009). The temperature is calculated by interpolating between pre-determined temperatures, T_n and T_{io}, ascribed to the state of fully neutral and fully ionized gas respectively as a function of the newly calculated fraction of ionized atomic hydrogen in the ith cell η_i:

$$T_i = T_n + \eta_i(T_{io} - T_n) \tag{7}$$

In this paper we use $T_n = 10\,\mathrm{K}$ and $T_{io} = 10000\,\mathrm{K}$ for all models that use this simplified thermal balance calculation.

2.4   Radiation Hydrodynamics

The hydrodynamics and photoionization schemes outlined in sections 2.1 and 2.3 are combined using operator splitting to perform radiation hydrodynamics calculations. A photoionization calculation is initially run to convergence, this generally allows subsequent calculations to run relatively quickly

given that they are usually minor perturbations of the previous state. We then perform photoionization and hydrodynamics steps sequentially. In this work, the photoionization calculation for a time step is always calculated prior to the hydrodynamics calculation.

This operator splitting technique is flexible and relatively conceptually straightforward. It is however very computationally expensive, requiring a large number of Monte-Carlo photoionization calculations that render the gravitational and hydrodynamic components of the calculation negligible in comparative computational cost. Fortunately, this approach can be efficiently parallelized.

2.5 Implementation

Despite the high computational cost of this radiation hydrodynamics scheme, it is extremely scalable. The computational domain is decomposed into subdomains over which the components of the radiation hydrodynamics calculation are computed by an individual processor (thread). In three dimensions subdomains take the form of cubes of equal volume, which at present can be either 1/8, 1/64 or 1/512 of the total domain volume. An additional master thread performs governing and collating operations, giving a total of 65 threads for each of the three-dimensional models performed here. At lower dimensionality the grid can be decomposed in a similar manner into equally sized squares (2D) or lines (1D).

In the photoionization component of a calculation, photon packets are communicated between threads in stacks rather than individually to reduce the communication latency overhead. TORUS stores quantities using an octree AMR grid however adaptive refinement and coarsening of the grid is not yet fully tested in the hydrodynamics routine, a fixed grid is therefore used for models in this work.

The RDI calculations presented in this paper were run on an SGI Altix ICE system using 65 2.83GHz Intel Xeon cores across 9 dual quad-core compute nodes. These typically completed within 600–1000 hours of wall time. The models that include the diffuse field do not necessarily take the longest time to complete, as the additional hydrodynamic and photoionization calculations required for models that develop the highest velocity material motions outweigh the additional time taken for each photoionization calculation when the diffuse field is included.

3 NUMERICAL TESTS

A number of tests have been conducted to confirm that TORUS is in agreement with accepted benchmarks. We treat the photoionization, hydrodynamics and self-gravity in isolation as well as the radiation hydrodynamics. Comprehensive tables of test parameters are provided to enable replication by other codes.

3.1 Photoionization: The HII40 Lexington Benchmark

The HII40 Lexington benchmark is a one dimensional test in which the equilibrium temperature and ionization structure of an HII region heated by a star at $40000\,\text{K}$ is calculated

Table 1. Lexington benchmark parameters.

Variable (Unit)	Value	Description
T_{eff} (K)	40000	Source effective temperature
R_* $(R_\odot)$	18.67	Source radius
n_{H} (cm^{-3})	100	Hydrogen number density
$\log_{10}(\text{He/H})$	-1	Helium abundance
$\log_{10}(\text{C/H})$	-3.66	Carbon abundance
$\log_{10}(\text{N/H})$	-4.40	Nitrogen abundance
$\log_{10}(\text{O/H})$	-3.48	Oxygen abundance
$\log_{10}(\text{Ne/H})$	-4.30	Neon abundance
$\log_{10}(\text{S/H})$	-5.05	Sulphur abundance
L (cm)	4.4×10^{19}	Computational domain size
n_{cells}	1024	Number of grid cells

and compared with the output of one of the many codes that reproduce the accepted result (see Ferland 1995). Here we calculate a comparison set of results using the one dimensional semi-analytic code Cloudy (Ferland et al. 1998), one of the original contributors to the benchmark. The system modelled comprises a star at $40000\,\text{K}$ at the left hand edge of the grid, size 4.4×10^{19}cm comprising 1024 cells. This test incorporates more species than only hydrogen and does not rely on the simplified thermal balance calculation of equation 7, rather the temperature of the cell is determined through comparison of the heating and cooling rates. It also includes treatment of the diffuse field.

A full list of parameters used for this benchmark is given in Table 1 and the resulting temperature and ionization fractions as calculated using both TORUS and Cloudy are shown in Figure 1. TORUS is consistent with the Cloudy temperature distribution to within 10% and is generally much better than this. The higher temperature calculated by TORUS in the inner regions is in agreement with the result obtained in Wood et al. (2004). The hydrogen and helium ionization fractions agree extremely well, this is of particular importance with regard to the hydrogen-only radiation hydrodynamics models in this paper. The other ions match to within similar levels of agreement as Ercolano et al. (2003) and Wood et al. (2004). Discrepancies in the result of this benchmark are usually attributed to differences in the atomic data used by the codes that are being compared.

3.2 Hydrodynamics Tests

3.2.1 Sod Shock Tube

The Sod shock tube test is a simple 1-dimensional model, initially comprising two equal volumes separated by a partition. Both partitions, the left hand partition (LHP) and right hand partition (RHP), contain ideal gases at zero velocity with different densities and hence different initial pressure and energy. At time $t = 0\,\text{s}$, the partition is removed and the system allowed to evolve. The state after a time t is detailed by Sod (1978).

We use an adiabatic equation of state, with adiabatic index $\gamma = 7/5$. Unless otherwise stated, a value of 0.3 is used for the Courant–Friedrichs–Lewy (CFL) parameter in all hydrodynamics models. In this model boundary conditions are reflective and 1024 cells are used for the grid.

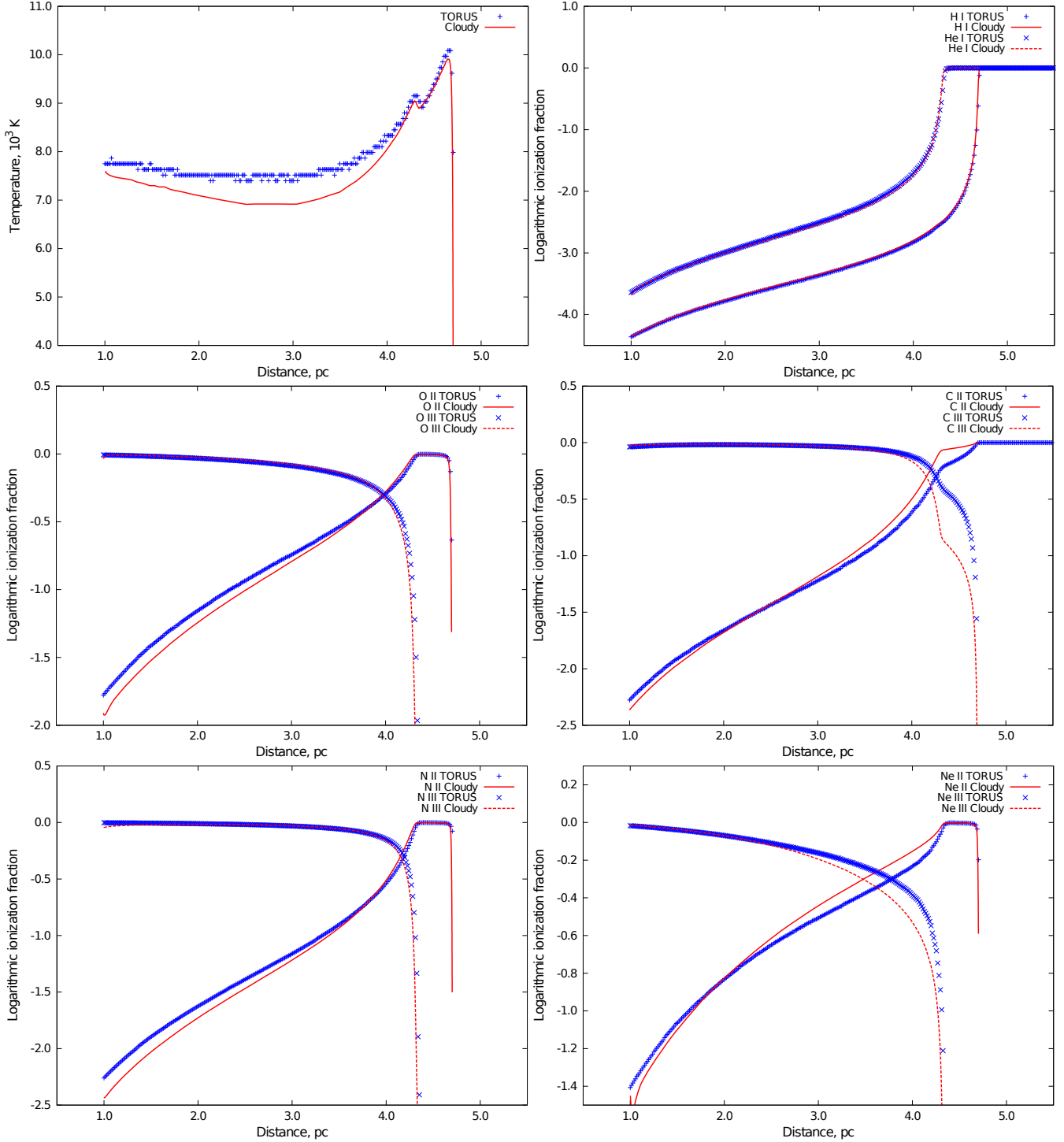A summary of the model parameters is given in Ta-

Figure 1. Top Left: The temperature distribution for the Lexington benchmark. Top Right: Hydrogen and helium ionization fractions. Middle Left: Oxygen ionization fractions. Middle Right: Carbon ionization fractions. Bottom Left: Nitrogen ionization fractions. Bottom Right: Neon ionization fractions.

ble 2 and the result as computed by TORUS at $t = 0.2\,\text{s}$ is shown in Figure 2. The features in this result are, from right to left; the initial density in the RHP, a shock wave which forms as a result of the low density material recoiling away from the high density material, a contact discontinuity between the high density material of the LHP and the low density material of the RHP, a rarefaction wave formed

because the contact discontinuity acts as a piston drawing left hand material to the right and the initial density of the LHP.

TORUS shows excellent agreement with the analytical solution. The slight density dip at the rarefaction wave–contact discontinuity interface arises because TVD flux limited schemes only smooth out oscillations near sharp shocks.

Table 2. Sod shock tube parameters.

Variable (Unit)	Value	Description
ρ_1 $(\mathrm{g\,cm^{-3}})$	1	Initial density in LHP
ρ_2 $(\mathrm{g\,cm^{-3}})$	0.125	Initial density in RHP
γ	7/5	Adiabatic index
P_1 $(\mathrm{dyn\,cm^{-2}})$	1	Initial pressure in LHP
P_2 $(\mathrm{dyn\,cm^{-2}})$	0.1	Initial pressure in RHP
E_1 $(\mathrm{erg\,cm^{-3}})$	2.5	Initial energy density in LHP
E_1 $(\mathrm{erg\,cm^{-3}})$	2.0	Initial energy density in RHP
E.O.S.	Adiabatic	Equation of state
L (cm)	1	Computational domain size
n_{cells}	1024	Number of grid cells

Table 3. Sedov-Taylor parameters.

Variable (Unit)	Value	Description
γ	7/5	Adiabatic index
v $(\mathrm{cm\,s^{-1}})$	0	Initial velocity
ρ $(\mathrm{g\,cm^{-2}})$	1	Initial surface density
r_{i} (cm)	0.01	Energy dump zone radius
E_{Blast} $(\mathrm{erg\,cm^{-2}})$	3183.1	Dump zone surface energy density
E_{o} $(\mathrm{erg\,cm^{-2}})$	1×10^{-5}	Ambient surface energy density
E.O.S.	Adiabatic	Equation of state
L(cm)	1	Computational domain size
n_{cells}	512^2	Number of grid cells

This is a necessary compromise, so that existing physical oscillations are not unphysically damped.
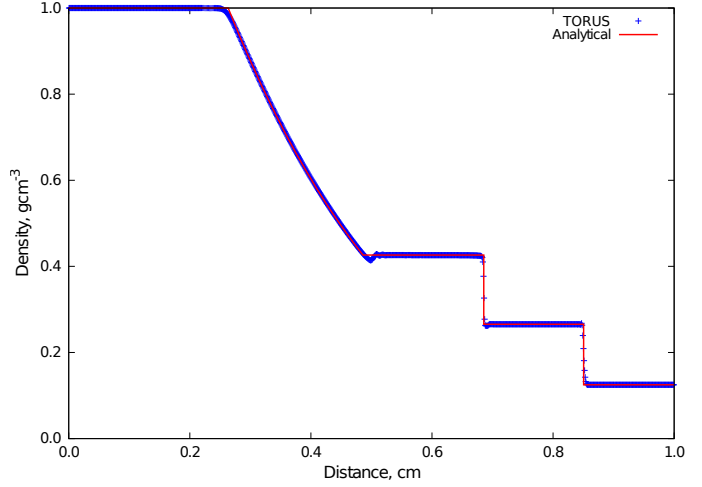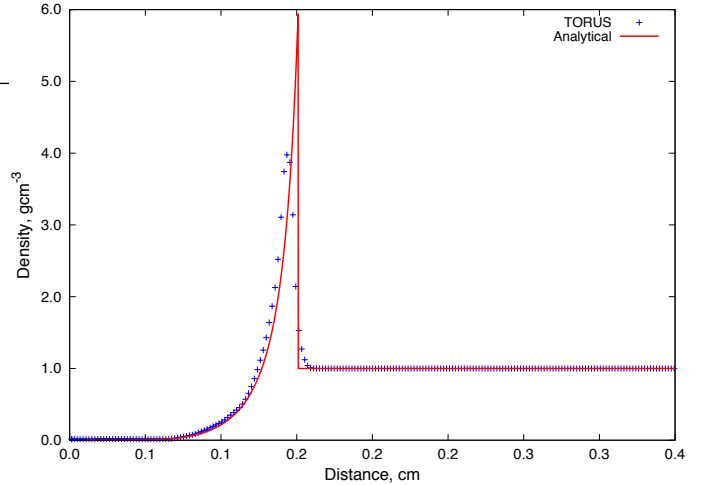
3.2.2 Sedov-Taylor Blast Wave

The Sedov-Taylor blast wave is an extreme model, which tests the advection scheme beyond the demands that will be made of it in star formation applications. In this 2-dimensional test a large amount of energy is injected into a circular region, radius 0.01 cm, of a constant density ideal gas, causing a blast wave. Self-similar analytical solutions for the time evolution of such a blast wave were found by Taylor (1950b) and Sedov (1946).

The initial ratio of thermal energy in the circular region to the rest of the grid is $3 \times 10^8 : 1$. Given the extreme nature of this model, a CFL parameter value of 0.08 was required in order to capture the early stages of evolution without numerical instability arising. The boundary conditions used in this test are all reflective and the grid comprises 512^2 cells. A full table of parameters is given in Table 3 and a comparison of the density distribution at time $t = 0.03\,\mathrm{s}$, as calculated both by TORUS and analytically, is given in Figure 3. TORUS demonstrates a good level of agreement with the analytical solution but, as with all numerical schemes, suffers from numerical diffusion. This is responsible for the slight broadening of the shock and reduction in the peak amplitude compared to the analytical solution.

3.2.3 Kelvin-Helmholtz Instability

Kelvin-Helmholtz (KH) instabilities are vortices that form at an interface between two materials due to shear forces (Von Helmholtz 1868; Kelvin 1871). Adaptations to SPH
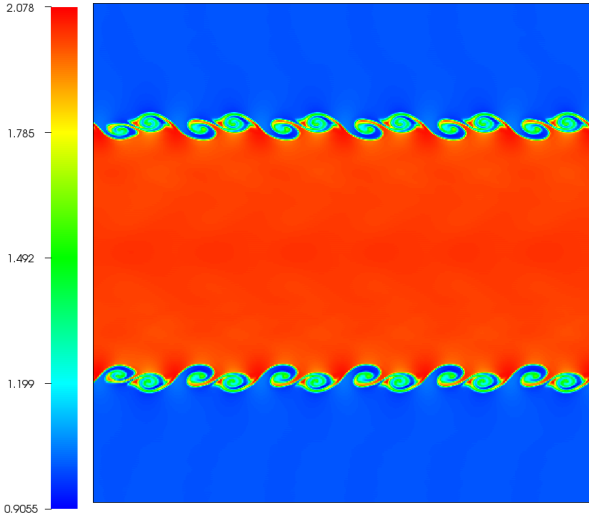
Figure 2. Density distribution of the Sod shock tube test at $t = 0.2\mathrm{s}$, showing both the result given by TORUS (blue crosses) and the analytical solution (red line).

Figure 3. Density distribution of the Sedov-Taylor blast wave at $t = 0.03\,\mathrm{s}$ showing both the result given by TORUS (blue crosses) and the analytical solution (red line).

codes have recently found to be required in order to form KH instabilities by Agertz et al. (2007) and Price (2008), thus reproducing these has proved to be an important test of hydrodynamical algorithms.

The 2-dimensional system modelled here follows Price (2008), comprising two fluids in contact at different density and velocity, such that the ratio of their densities is 2:1 and their velocities are equal in magnitude but in opposite directions. Periodic boundary conditions are used at the $\pm x$ boundaries and reflective conditions at the $\pm z$ boundaries, corresponding to housing the system in a pipe that extends indefinitely in $\pm x$. At time $t = 0\,\mathrm{s}$ the interface between these fluids is subject to a perturbation of the form

Table 4. Kelvin-Helmholtz parameters.

Variable (Unit)	Value	Description
γ	5/3	Adiabatic Index
ρ_1 $(\mathrm{g\,cm^{-2}})$	1	Ambient fluid initial surface density
ρ_2 $(\mathrm{g\,cm^{-2}})$	2	Central fluid initial surface density
u_1 $(\mathrm{cm\,s^{-1}})$	-0.5	Ambient fluid initial velocity
u_2 $(\mathrm{cm\,s^{-1}})$	$+0.5$	Central fluid initial velocity
E.O.S	Adiabatic	Equation of State
A	0.025	Constant in perturbation equation
λ (cm)	1/6	Wavelength of perturbation
L (cm)	1	Computational domain size
n_{cells}	512^2	Number of grid cells

Figure 4. Surface density distribution in $\mathrm{g\,cm^{-2}}$ at τ_{KH} across the $1\mathrm{cm}^2$ domain of the Kelvin-Helmholtz instability model.

$$u = \begin{cases} A\sin(-2\pi(\mathrm{x}+1/2)(1/6)), & |z-0.25| < 0.025 \\ \\ A\sin(2\pi(\mathrm{x}+1/2)(1/6)), & |z+0.25| < 0.025. \end{cases} \quad (8)$$
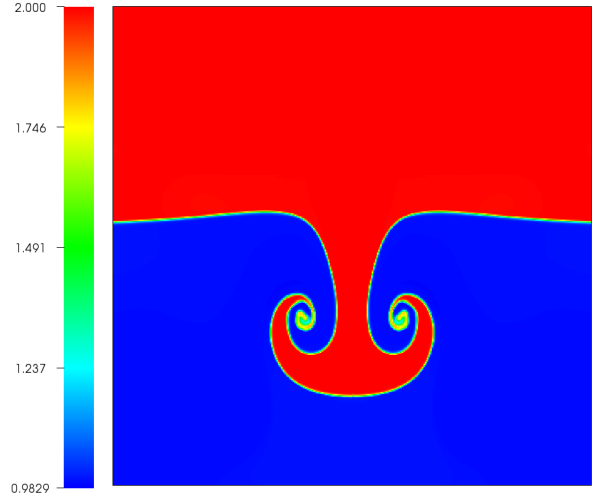
vortices should then form within a characteristic KH timescale given by

$$\tau_{KH} = \frac{2\pi}{\omega}. \quad (9)$$

Where, for materials in contact with density ρ_1 and ρ_2 and velocities v_1 and v_2 subject to a periodic perturbation of wavelength λ

$$\omega = \frac{2\pi}{\lambda} \frac{(\rho_1\rho_2)^{1/2}|v_1 - v_2|}{(\rho_1 + \rho_2)}. \quad (10)$$

A full table of parameters used for this test is given in Table 4. Using these parameters and equations 9 and 10 we obtain a KH timescale of approximately 0.35 seconds, the time within which vortices should form. A plot of the density distribution as calculated by TORUS at τ_{KH} is given in Figure 4 and clearly demonstrates that primary and secondary vortices have formed within the KH timescale. This test has also been successfully performed using density ratios of 5:1 and 10:1.

Figure 5. Surface density distribution in $\mathrm{g\,cm^{-2}}$ showing the 'mushroom' formed in our $1\,\mathrm{cm}^2$ domain size, Rayleigh-Taylor instability model. It comprises a penetrating column of material with Kelvin-Helmholtz instabilities forming where the materials flow past one another.

3.2.4 Rayleigh-Taylor Instability

Rayleigh-Taylor instabilities can arise where a material is 'on top' of a second lower density material in a gravitational potential and the interface between them is subject to a perturbation (Rayleigh 1900; Taylor 1950a). They are manifested as 'Rayleigh-Taylor fingers' that propagate into the low density material along which Kelvin-Helmholtz instabilities may form. This gives rise to a characteristic mushroom shape. In the following test we have selected system parameters that should give rise to this characteristic structure.

At time $t = 0\,\mathrm{s}$ the interface between two different density materials in a $1\,\mathrm{cm}^2$ box in the presence of a gravitational field is subject to a small disturbance of magnitude $-0.055\,\mathrm{cm\,s^{-1}}$ across a finite range $0.45 < x < 0.55$ of the interface, the system is then left to evolve. We use periodic boundary conditions at the $\pm x$-direction bounds and reflective at the $\pm z$-direction bounds. The gravitational potential ϕ at height z is given by

$$\phi(z) = gz \quad (11)$$

where g is the acceleration due to gravity, here equal to $0.1\,\mathrm{cm\,s^{-2}}$.

A summary of parameters used in this test is given in Table 5. Figure 5 shows the distinctive mushroom-shape formed via this method at time $t = 5\,\mathrm{s}$. The main body of the mushroom is the Rayleigh-Taylor finger, at the tip of which Kelvin-Helmholtz instabilities have formed.

3.3 Self-Gravity

This test follows, in three dimensions, the collapse of an initially uniform sphere to form an $n = 1$ polytrope. A polytropic cloud is one in which the pressure P varies according to the following relation:

Table 5. Rayleigh-Taylor parameters.

Variable (Unit)	Value	Description
ρ_1 (g cm^{-2})	2	Surface density of upper material
ρ_2 (g cm^{-2})	1	Surface density of lower material
g (cm s^{-2})	0.1	gravitational acceleration
E.O.S.	Adiabatic	Equation of state
L (cm^2)	1	Computational domain size
n_{cells}	512^2	Number of grid cells

Table 6. Self-gravity test parameters.

Variable (Unit)	Value	Description
M_{sphere} ($M_\odot$)	1	Mass of initial sphere
r_{sphere} (pc)	1	Radius of initial sphere
γ	2	Adiabatic index
E.O.S.	Polytropic	Equation of state
K	4.1317×10^{29}	Equation 12 constant
n_{cells}	128^3	Number of grid cells

$$P = K\rho^{1+\frac{1}{n}} \tag{12}$$

where n is the index of the polytrope, ρ is the density and K is a constant.

The corresponding solution to Poisson's equation for a self-gravitating polytropic fluid is given by the Lane-Emden equation, which details the variation in pressure and density in terms of dimensionless variables ζ and θ:

$$\frac{1}{\zeta^2}\frac{d}{d\zeta}\left(\zeta^2\frac{d\theta}{d\zeta}\right) + \theta^n = 0. \tag{13}$$

θ and ζ are given by equations 14 and 15:
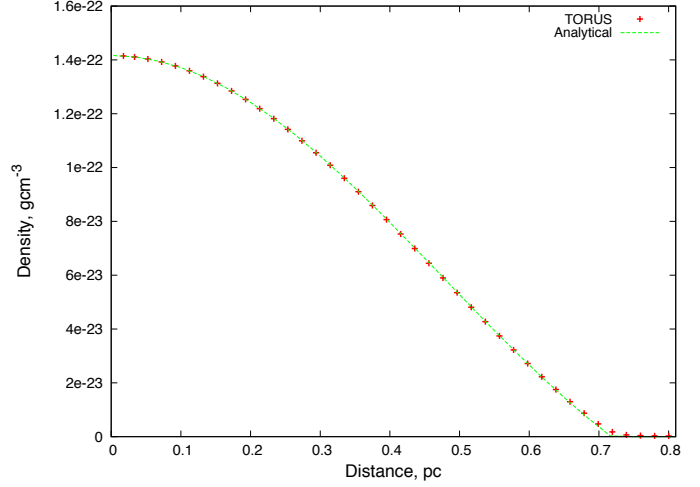
$$\theta^n = \frac{\rho}{\rho_c} \tag{14}$$

and

$$\zeta = r\left(\frac{4\pi G\rho_c^2}{(n+1)P_c}\right)^{1/2} \tag{15}$$

where r, ρ_c and P_c are the radial position, central density and pressure respectively.

The solution to the Lane-Emden equation for an $n = 1$ polytrope is simply a sinc function, which should be the form of the resulting density distribution once collapse has occurred. We employ reflecting boundary conditions. A summary of the parameters used for this test is given in Table 6. We ran the model with significant artifical viscosity in order to strongly damp the oscillations that would otherwise occur. The resulting radial density distribution as calculated both analytically and by TORUS is given in Figure 6 and demonstrates that TORUS is in excellent agreement with the expected result.

3.4   Radiation Hydrodynamics: Expansion of an HII region

The time evolution of the extent of an HII region around, for example, an O-type star can be divided into two regimes. First note that using a time-independent, photoionization equilibrium consideration, the HII region extends until the

Figure 6. The analytical and TORUS-computed resulting density distribution for the collapse of a uniform density sphere to form an $n = 1$ polytrope.

rates of ionization and recombination become equal. In a uniform density, hydrogen-only, isotropic medium this corresponds to a spherical HII region with extent r_I^o known as the 'Strömgren radius', given by:

$$r_I^o = \left(\frac{3N_\gamma}{4\pi n_e^2\alpha^{(2)}}\right)^{1/3} \tag{16}$$

Where N_γ is the number of ionizing photons from the source per second, n_e is the electron number density and $\alpha^{(2)}$ is the recombination coefficient into all states except the ground state.

In the time-dependent case the first phase of evolution is that in which $r_I < r_I^o$. Here, the expansion is initially very rapid. Since the surrounding material near the star can be assumed to be ionized as soon as the stellar radiation reaches it, the ionization front propagates at the speed of light over a mean free path. Given that the ionizing front propagates much more rapidly than the speed of sound c_s little subsequent material motion occurs.

In the second phase of evolution, the hot ionized region expands into the surrounding, cool, material as a consequence of the pressure difference between them. Once the ionization front expansion velocity drops below c_s, a shock moves ahead of the ionization front into the neutral material. Spitzer (1978) showed that the analytical radius of an HII region in the phase two expansion at time t is given by
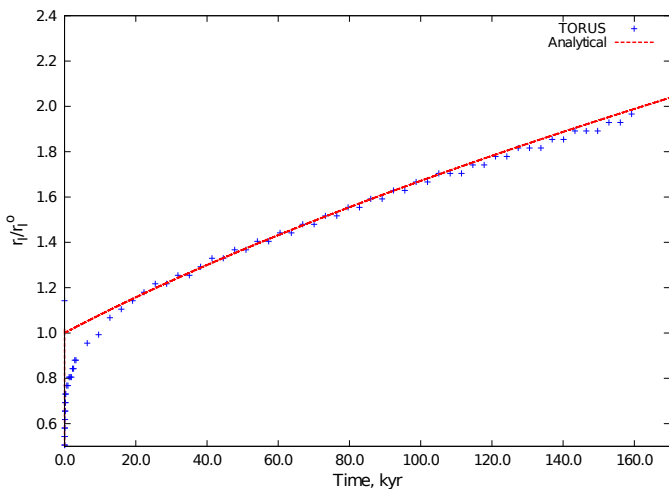
$$r_I = r_I^o\left(1 + \frac{7}{4}\frac{c_I t}{r_I^o}\right)^{4/7} \tag{17}$$

up until the point where pressure equilibrium is approached, where c_I is the speed of sound in the ionized gas. Equation 17 is constructed using the thin shell approximation.

In this test the second phase expansion is modelled in three dimensions, using equation 17 as a comparison. The evolution of the first phase expansion, prior to r_I^o, is ignored

Table 7. Parameters used for the HII expansion model.

Variable (Unit)	Value	Description
$\rho_{\rm o}$ (m$_{\rm H}$ cm^{-3})	100	Initial density
$T_{\rm o}$ (K)	10	Initial temperature of grid
$u_{\rm o}$ (cm s^{-1})	0	Initial velocity throughout grid
γ	5/3	Adiabatic index
E.O.S	Isothermal	Equation of state
T_* (K)	40000	Effective source temperature
R_* (R$_\odot$)	10	Source radius
L(pc^3)	11.36	Grid size
$n_{\rm cells}$	128^3	Number of grid cells

Figure 7. The position of the ionization front with time from $r_{\rm I} = r_{\rm I}^{\rm o}$

because the calculations here assume photoionization equilibrium. The system consists of a star at $40000\,\rm K$ with a blackbody spectrum at the centre of a $4\,\rm pc^3$ box of neutral hydrogen with reflective boundary conditions. We perform a radiation hydrodynamics calculation as outlined in section 2 and follow the evolution of the ionization front position, defined as the point where the atomic hydrogen ionization fraction $X(\rm HI) = 0.5$, from $r_{\rm I} = r_{\rm I}^{\rm o}$ with time.

Table 7 lists the parameters used in this test and the results are shown in Figure 7. TORUS shows excellent agreement with equation 17 shortly after reaching the Strömgren radius. (The discrepancies at early times occur because TORUS evolves from a neutral starting point whereas the analytical solution starts with the ionization front at the Strömgren radius). At late times the evolution starts to deviate from the analytical solution as sufficient material is accumulated for the thin shell approximation to no longer apply.

3.5 Testing Summary

We have shown that TORUS satisfies a number of benchmark tests. The radiative transfer scheme, including treatment of the diffuse field, is in good agreement with the Lexington benchmark as calculated by Cloudy (Ferland et al. 1998). The hydrodynamics algorithm satisfies the Sod shock tube test and Sedov-Taylor blast wave density distribu-

tions at a given point in time and has also been shown to produce Kelvin-Helmholtz and Rayleigh-Taylor instabilities. Furthermore our self-gravity calculation reproduces the same $n = 1$ polytropic density distribution as given by the Lane-Emden equation following the collapse of a uniform density sphere. Finally, the radiation hydrodynamics scheme has been shown to agree with the analytical work of Spitzer (1978) for the rate of expansion of an HII region. These results verify that TORUS hydrodynamics and photoionization modules reproduce the standard radiation and hydrodynamical benchmarks and is therefore ready for application to new problems.

4 RADIATIVELY DRIVEN IMPLOSION OF A BONNOR-EBERT SPHERE

Here we model the radiatively driven implosion of a Bonnor-Ebert sphere (a sphere in which the density varies according to equation 13) using three different treatments of the radiation field so as to distinguish their relative contributions to the evolution of the system. The three different radiation fields used are:

a) a monochromatic radiation field with the OTS approximation

b) a polychromatic radiation field with the OTS approximation

c) a polychromatic radiation field with the diffuse field, as outlined in section 2.3.

The details of the system are very similar to that of Gritschneder et al. (2009). A Bonnor-Ebert sphere of radius $1.6\,\rm pc$ resides at the centre of a $1.5 \times 10^{19}\,\rm cm^3$ ($4.87\,\rm pc^3$) grid of 128^3 cells. Our model domain is slightly larger than that used by Gritschneder et al. (2009) so that the evolution of larger extent of any shadowed region can be studied. The BES has a core number density of $10^3 \rm cm^{-3}$, with the material surrounding the BES having a number density equal to that at the BES edge (such a BES is known as 'incomplete'). The resolution of these models is currently limited by computational cost, however the number of grid cells here is equivalent to that used in the successful HII-region expansion test of section 3.4. This model is also on a smaller length scale than that of the HII-region expansion test so the resolution will be sufficiently high. As mentioned in section 2.5, we will be implementing an AMR grid that will enable the calculation of models at higher resolutions in future work.

The primary photon source is a star that lies outside the grid in the $-x$ direction. The radiation field is assumed to enter the grid plane parallel at the $-x$ boundary, at which photon packets are initiated at random locations and the flux is modified to account for geometric dilution.

As well as considering the three different radiation schemes mentioned above, we also treat the three different flux regimes considered in Gritschneder et al. (2009). These are denoted high, medium and low flux and correspond to the BES being located just within, on the edge of and just beyond the Strömgren radius respectively. The fluxes and corresponding stellar properties that were used to generate these different flux regimes are given in Table 8, along with the other parameters used for this model.

In all of the models presented here, the hydrodynamic boundary conditions are periodic at $\pm y$ and $\pm z$

Table 8. Parameters used for the RDI of a BES model.

Variable (Unit)	Value	Description
R_c (pc)	1.6	Cutoff radius
n_{max} (cm^{-3})	1000	Peak BES number density
T_o (K)	10	Initial temperature of grid
γ	1	Adiabatic index
E.O.S	Isothermal	Equation of state
Φ_{lo} (cm^{-2})	9.0×10^8	Low ionizing flux
D_{lo} (pc)	$(-10.679, 0, 0)$	Source position (low flux)
Φ_{med} (cm^{-2})	4.5×10^9	Intermediate ionizing flux
D_{med} (pc)	$(-4.782, 0, 0)$	Source position (medium flux)
Φ_{hi} (cm^{-2})	9.0×10^9	High ionizing flux
D_{hi} (pc)	$(-3.377, 0, 0)$	Source position (high flux)
L(pc^3)	4.87	Grid size
n_{cells}	128^3	Number of grid cells
CFL	0.3	CFL parameter

and free outflow/no inflow at $\pm x$. Dirichlet boundary conditions are used for the self-gravity calculation and the radiation field boundaries are free outflow/no inflow. Using this boundary condition for the radiation field can lead to reduced sampling at the domain boundaries, where material will be subject to non-symmetric diffuse flux.

The free fall time for this cloud is approximately 3 Myr, estimated using $1/(\sqrt{G\rho_{max}})$ where ρ_{max} is the central density and G is the gravitational constant. This is a factor of 15 longer than the total simulation time of 200 kyr. Radiation hydrodynamics will thus dominate gravitational effects in the evolution of the system. We dump the state of the computational grid every 5 kyr.

4.1 Results and Discussion

4.1.1 Initial properties

The initial ionization state of the system for all three flux regimes and photoionization schemes is shown in Figure 8. At this stage there is already a noticeable difference between them in the extent of their un-ionized regions. The top row from Figure 8 represents the starting point that would be obtained by most pre-existing models (specifically, it is a zoomed out version of Gritschneder et al. 2009). The middle row is the start point for the models in which a polychromatic radiation field is considered, but the OTS approximation is still applied. In comparison with the top row, it is clear that the extent of the ionized region has increased slightly and the transition region has been smoothed out. This is due to hard radiation, which penetrates more deeply since the photoionization cross section approximately decreases in proportion to the inverse cube of the photon frequency (Osterbrock 1989). The bottom row is the starting HI fraction for the models that include the diffuse field. In all three flux regimes the extent of the ionized region is significantly different to that of the other two sets of models. At high flux material in the wings of the model is completely ionized, the medium flux model I-front has significantly wrapped itself around the BES and the low flux model I-front now grazes the BES. Note that the curved I-front wings towards the edge of the low and medium flux models arise because these models

do not include periodic photon packet boundary conditions and so these regions are subject to a non-symmetric diffuse ionizing flux.

The logarithmic density distribution for the high, medium and low flux models over all three treatments of the radiation field, are shown side by side at 50, 100, 150 and 200 kyr in Figures 9, 10 and 11 respectively. In each of these figures the monochromatic models are represented by the left hand column, the polychromatic models by the central column and the polychromatic-diffuse models by the right hand column. It is clear that there are some marked differences between the evolutions of the system under the different radiation treatments. A case-by-case study of the evolution of the separate models is given below in sections 4.1.3, 4.1.4 and 4.1.5.

4.1.2 The formation and evolution of instabilities

A number of the models presented here are subject to the formation of instabilities. These arise when the thin shell swept up by the ionization front propagates though the lower density regions of the computational domain such as in the wings or (in the low flux regime) prior to driving into the BES.

There are two main sources of perturbation that may seed these instabilities. The first is 'angle of incidence' Williams (2002) in which regions of the I-front that are not entirely perpendicular to the incoming radiation field are subject to varying ionizing flux and therefore differential acceleration. This may occur as the I-front wraps around the BES. The second is numerically induced perturbation via noise in the calculated ionization fraction. As mentioned in section 2.3 the induced temperature, and therefore pressure, is directly proportional to the calculated ionization fraction (equation 7). The resulting pressure gradient then determines the induced advecting velocity. If a thin shell of material does not encounter any disruption in its propagation (like encountering a high density component of a BES) then even a small amount of numerical spread in the ionization fraction along the I-front will eventually lead to it bending on small scales and therefore induce thin shell instabilities (Vishniac 1983; Garcia-Segura & Franco 1996). Once the I-front structure is disrupted, the faster propagating components will lose mass by transfer to the cool neutral neighboring material perpendicular to the direction of the I-front propagation. This leads to an accumulation of material ahead of the slower moving components of the I-front, which further brakes the expansion in these regions. This transport of material also reduces the density in the faster moving components of the I-front, allowing photoionizing radiation to propagate more deeply (c.f. equation 16) and accelerate these components of the front further. Improving the accuracy of the ionization fractions in the front will delay the onset of numerically induced instabilities, however they should eventually arise for any non-analytical radiation hydrodynamics code if the I-front is allowed to propagate for long enough without being disrupted by some other means.

It is clear that other radiation-hydrodynamical methods should also seed these instabilities. For example, combining
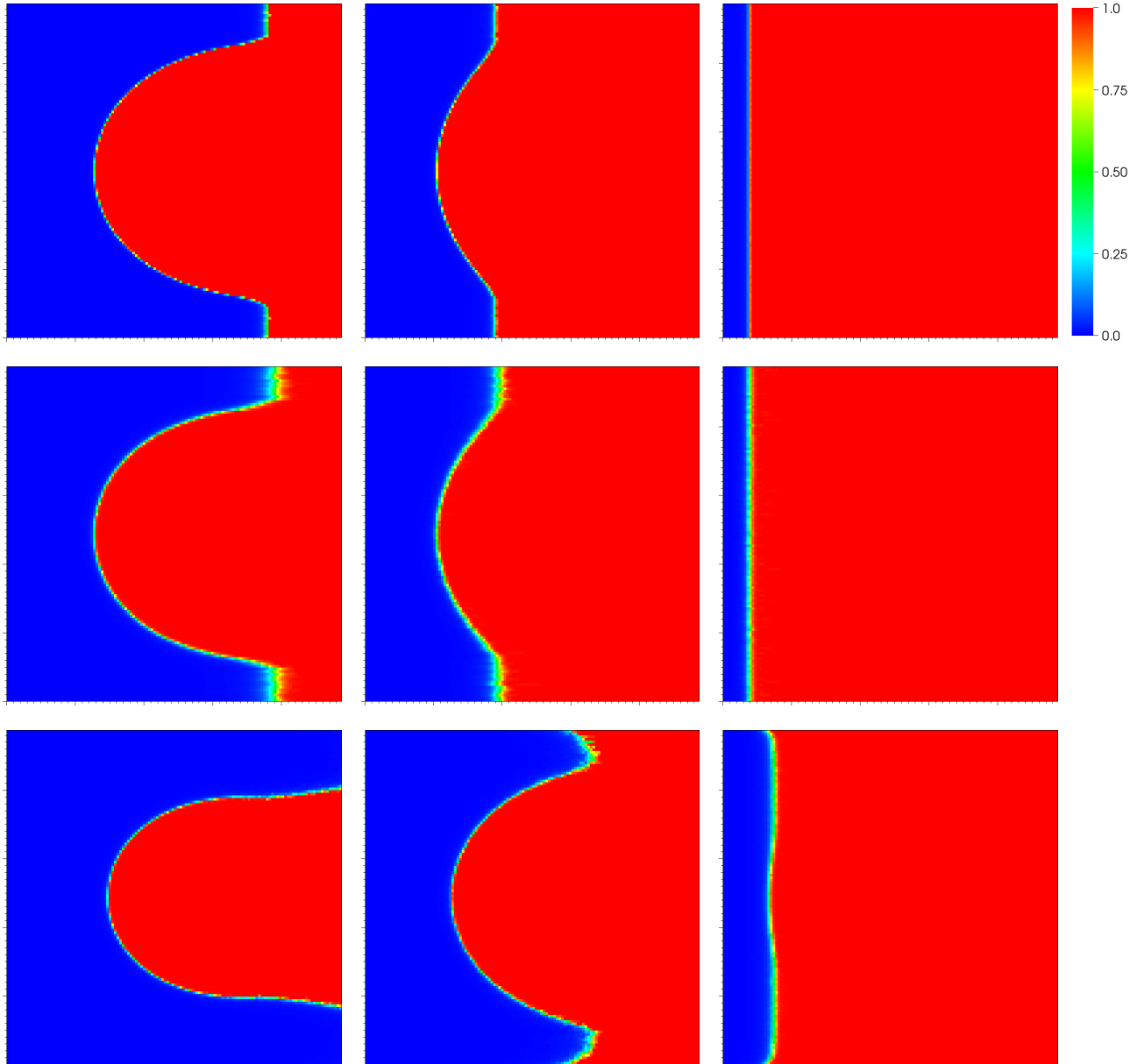
Figure 8. Top row) The hydrogen ionization fraction for the OTS monochromatic model. Middle row) The hydrogen ionization fraction for the OTS polychromatic model. Bottom row) The hydrogen ionization fraction for the model which includes the diffuse field. Columns are, from left to right, high, medium and low flux regimes. Each frame is a slice through the computational grid, which is a cube with sides 4.87 pc long. Major ticks are separated by 1 pc.

SPH hydrodynamics with ray-tracing will lead to a 'noisy' I-front due to the random-variation of the SPH representation of the density field. Grid-based codes with ray-tracing radiation-transfer will also be susceptible to instabilities as the angular sampling of the radiation field may not coincide perfectly with the axes of the underlying hydrodynamical grid. Of course within star forming regions themselves density perturbations will inevitably lead to the growth of instabilities.

Regardless of the seed of these instabilities in the simulations, their evolution occurs in a manner consistent with the instability studies referenced above and result in 'elephant trunk' structures. Their evolution also highlights in-

teresting differences between the different treatments of the radiation field, the details of which are discussed in the following sections.

4.1.3　High flux models

The high flux density evolutions are given in Figure 9 and broadly exhibit two different behaviours. In the polychromatic OTS and polychromatic-diffuse models the system is initially ionized to the extent that a strong shock cannot form quickly enough to effectively drive into the BES. What material is accumulated propagates for a short time until the higher density BES brakes it and a photo-evaporative flow is
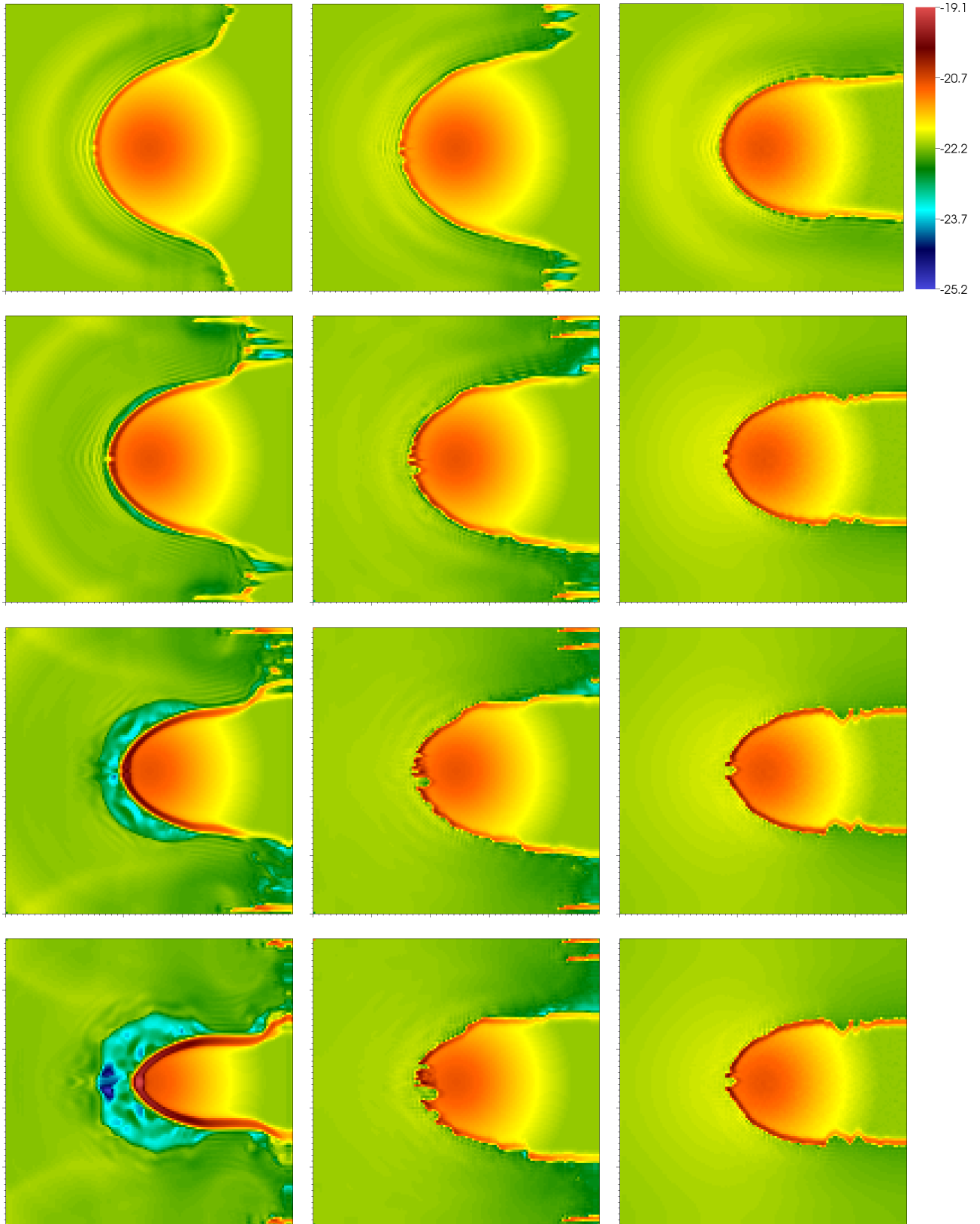
Figure 9. The high flux model logarithmic density distributions (cgs). Left column) Monochromatic models. Middle column) Polychromatic models. Right column) Polychromatic-diffuse models. Time is increasing from top to bottom, with snapshots at 50, 100, 150 and 200 kyr. Each frame is a slice through the computational grid, which is a cube with sides 4.87 pc long. Major ticks are separated by 1 pc.
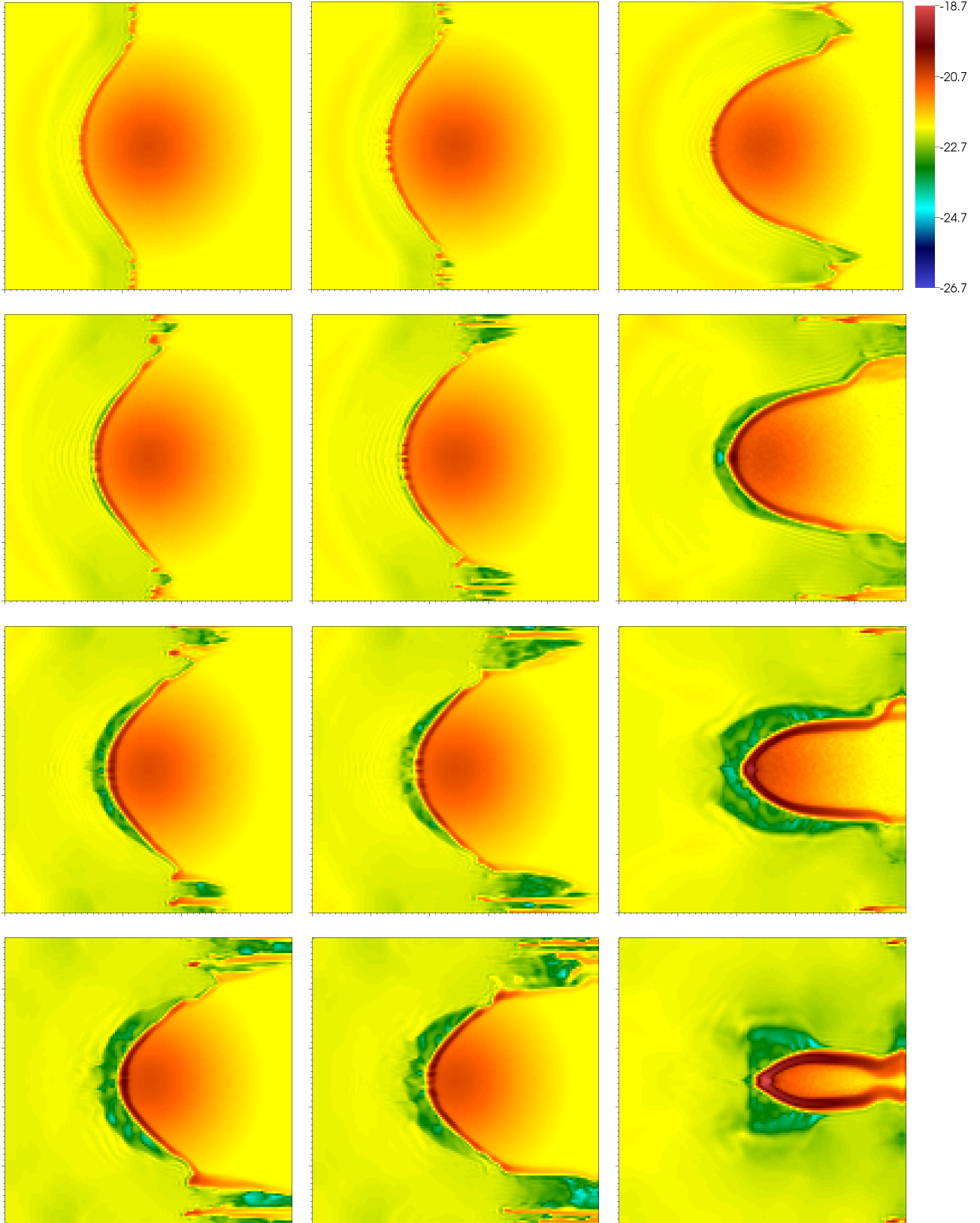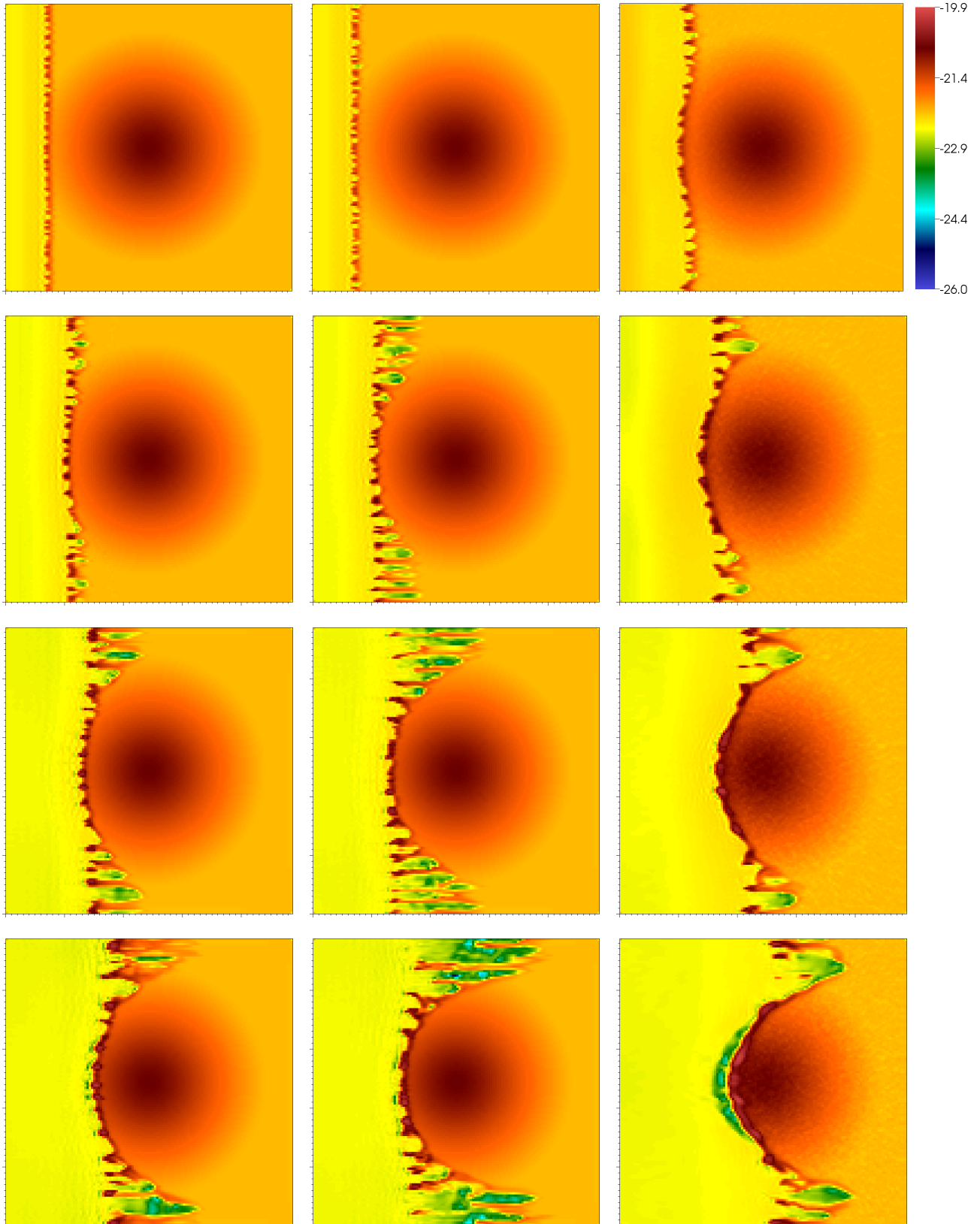
Figure 10. The medium flux model logarithmic density distributions (cgs). Left column) Monochromatic models. Middle column) Polychromatic models. Right column) Polychromatic-diffuse models. Time is increasing from top to bottom, with snapshots at 50, 100, 150 and 200 kyr. Each frame is a slice through the computational grid, which is a cube with sides 4.87 pc long. Major ticks are separated by 1 pc.

Figure 11. The low flux model logarithmic density distributions (cgs). Left column) Monochromatic models. Middle column) Polychromatic models. Right column) Polychromatic-diffuse models. Time is increasing from top to bottom, with snapshots at 50, 100, 150 and 200 kyr. Each frame is a slice through the computational grid, which is a cube with sides 4.87 pc long. Major ticks are separated by 1 pc.

established (Bertoldi & McKee 1990). The evolution of the resulting structure is then a consequence of rocket motion as heated, dense, material is evaporated away from the surface of the cloud into the low density external material (Oort & Spitzer 1955). The tunnelling of material at the tip and along the length of these models into the cometary structure occurs where there are differences between rocket-motion velocities due to either variations in the accumulated density or the density internal to the shell. An interesting difference between the OTS and diffuse field models is also revealed in the rocket-driven phase, with the OTS model being accelerated only along components facing the ionizing source and the diffuse field model being accelerated across the entire cometary surface due to diffuse-driven photo-evaporation.

On the other hand, the monochromatic OTS model does form a strong shock sufficiently rapidly to effectively drive into the BES, this leads to greater compression and accumulation of material into a relatively thick shell around the edge of the resulting bow structure. To illustrate the early braking of the polychromatic models, the difference in the velocity field between the monochromatic OTS and diffuse models at 50 kyr is illustrated in Figure 12. At this point the monochromatic model is still driving a shock into the BES and accumulating material, whereas the polychromatic-diffuse model is beginning a photo-evaporative flow.

In the OTS model, sufficient material is rapidly accumulated for a short, strong, photoevaporative flow to occur prior to substantial braking of the bow. The resulting rocket-motion is therefore much stronger than normal photoevaporative flow, giving rise to the ejection of a significant amount of material that accelerates the existing shock and carves out a low density wake. Subsequent ejections also occur episodically along the length of the bow that is exposed to ionizing radiation. The result is a disrupted region surrounding the tip of the bow structure in which densities can be excavated to levels lower than the ambient surroundings. A possible cause of the episodic nature of this process is that the outer shell density oscillates about some critical value as the shell sequentially accumulates and ejects. This 'episodic photo-evaporative ejection' further drives the collapse very effectively and contracts the bow perpendicularly to the ejection direction, tapering the head of the cometary structure. Figure 13 shows the disrupted region around the tip of the bow of the monochromatic model at 180, 185 and 190 kyr and illustrates the motion of discrete knots of material away from the surface, rather than a continuous stream.

The evolution of the maximum cell densities for each high flux model are shown in the top frame of Figure 14. This can be used in conjunction with the appropriate density map to illustrate the rate at which material is collected. Here the maximum density evolution highlights the differences between the two different behaviours noted above. In the polychromatic and polychromatic-diffuse models the maximum density increases at a declining rate and eventually plateaus. The monochromatic model continues accumulating material as it is effectively rocket-driven towards the core of the BES, finishing with a maximum density approximately 4.5 times that of the other models. Star formation at this flux regime will actually occur more slowly when polychromatic radia-
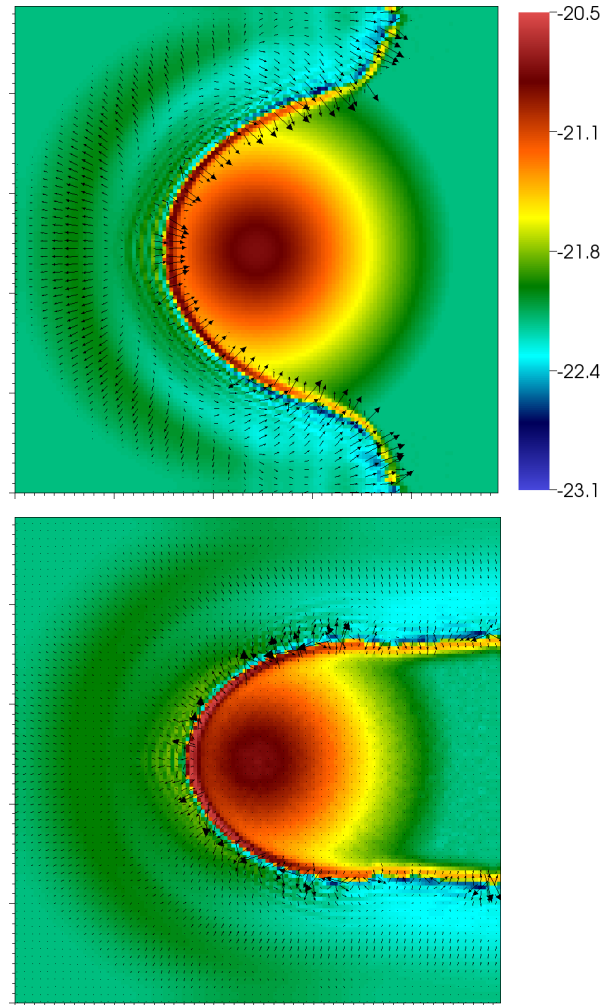

Figure 12. The logarithmic density field in $g\,cm^{-3}$, with velocity vectors, for the high flux models at 50 kyr. This demonstrates the difference between the driving shock of the monochromatic OTS model (top frame) and the photo-evaporative flow of the polychromatic-diffuse model (bottom frame). Each frame is a slice through the computational grid, which is a cube with sides 4.87 pc long. Major ticks are separated by 1 pc. Typical shock (upper frame) and outflow (lower frame) velocities are 5-7 $km\,s^{-1}$ and 1-4 $km\,s^{-1}$ respectively.

tion or the diffuse field is accounted for than in the simplified calculation.

The formation of thin shell instabilities has little to no impact in the evolution of these models, appearing only in the wings of the polychromatic and monochromatic OTS models and are simply swept off the grid.

4.1.4 Medium flux models

The medium flux density evolution is presented in Figure 10 and exhibits the largest difference between the final states of the OTS and diffuse field models. The OTS models both develop shocks that drive effectively into the BES, resulting in rapidly formed high density bow structures. The accumulated density is high enough to give rise to a scaled down version of the episodic photo-evaporatively driven collapse exhibited by the high flux monochromatic model and leads
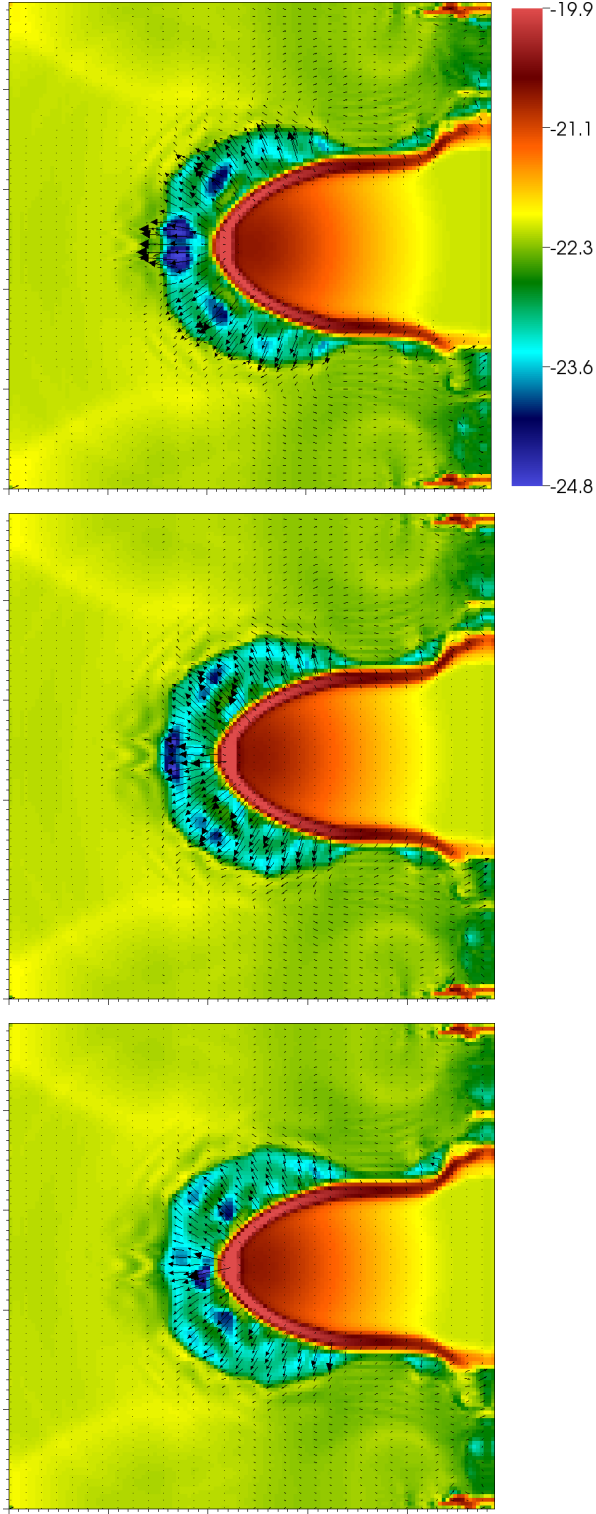
Figure 13. Logarithmic density snapshots in $g\,cm^{-3}$ with velocity vectors for the high flux monochromatic model at 180, 185 and 190 kyr. This illustrates the ejection of distinct knots of material and the evolution of the disrupted region around the tip of the bow. Each frame is a slice through the computational grid, which is a cube with sides 4.87 pc long. Major ticks are separated by 1 pc. Typical velocities in the outflow region of each frame are 25-35 $km\,s^{-1}$.
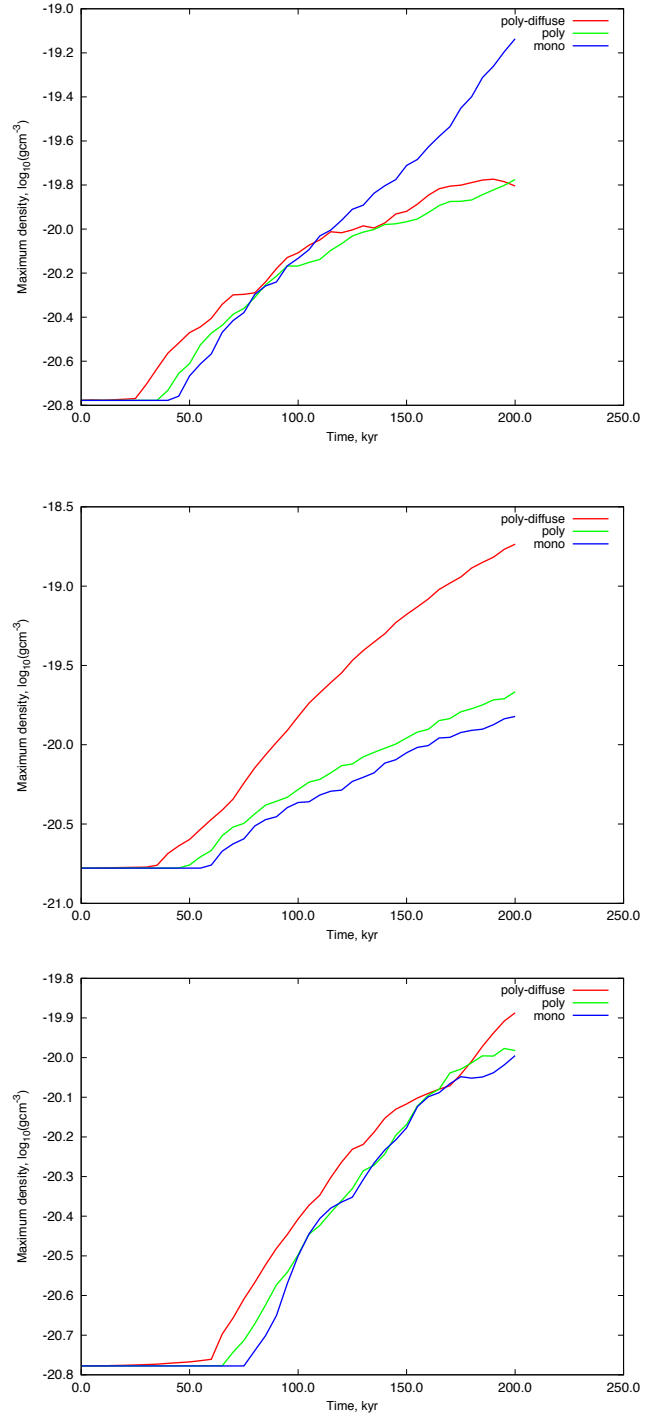

Figure 14. The evolution of maximum logarithmic densities respectively. Flux regimes are high to low from top to bottom.

to the same rocket-motion that continues driving material towards the centre of the BES and tapers the bow head. In the wings of the OTS models instabilities form via the mechanism described in section 4.1.2 and propagate linearly, having no effect of the rate of collapse and eventually being swept off of the grid. Note that the low density regions in the wake of these instabilities are not due to photo-evaporative

flow, rather they have been excavated by the high velocity instability shocks, with the material funnelled laterally to form knots and elephant trunks.

The diffuse field model behaves slightly differently, resembling a more effectively collapsed version of the monochromatic OTS high flux model. Again a strong shock is developed which drives into the BES and transitions to episodic photo-evaporatively driven collapse. The major difference lies in the wings of the model, which effectively drive into the side of the BES resulting in a final bullet-like structure with a very high density at what was the core of the BES. The reason for this is that a photo-evaporative flow can establish itself along a greater extent of the bow, into regions that would otherwise be shadowed from heating, because of the diffuse radiation field. This results in a whip-like progression of photo-evaporation along the trunk as the shell sequentially becomes dense enough to readily eject material and ceases in the tail regions when the diffuse ionizing flux becomes too low to cause heating. This will most likely result in much more rapid star formation in the model that includes the diffuse field. The evolution of the maximum cell density for these medium flux models is shown in the middle frame of Figure 14. This clearly highlights the fairly extreme difference between the OTS and diffuse field models, with a final difference in maximum density at 200 kyr of well over a factor of 10.

4.1.5 Low flux models

The low flux density evolutions are given in Figure 11. These models exhibit the largest susceptibility to thin shell instability as instabilities can begin developing across the entirety of the I-front before it impacts the BES. Instabilities that collide with the BES are braked and result in high density knots along the rim of the resulting bow structure. Those that continue in the wings of the model are elongated into elephant trunks with high density tips via the mechanism described in section 4.1.2. The evolution of these elephant trunks varies with each treatment of the radiation field. The polychromatic OTS trunks are more elongated than the monochromatic ones because hard radiation carves out a path more rapidly. Any compression of the trunks in the OTS models is due to thermal pressure. In the polychromatic-diffuse model, diffuse field radiation effectively drives into the material perpendicular to any displacement in the ionization front and therefore actually prevents the formation of a number of potential trunks by smoothing out dimples. Those trunks that do form will also continue to be both compressed thermally and exposed to diffuse ionizing radiation.

The RDI process for the OTS models occurs very weakly, with more material being accumulated through instability than compression. The diffuse field model drives into the BES more effectively, forming a smoother high density bow compared to the knotted structures of the other models and manages to initiate some photo-evaporative flow. The maximum cell density evolution for the low flux models is given in the bottom frame of Figure 14. At 200 kyr the diffuse field model has accumulated only a slightly larger maximum density than the OTS models, though it is clear from Figure 11 that it has achieved this order of density over a relatively large volume. The diffuse field model will most

likely form stars first and on a larger scale than the models that use the OTS approximation.

These low flux results, comprising a bright rimmed cloud with pillars along its wings, bear resemblance to observed systems such as IC 1848E, as shown in Figure 1 of Chauhan et al. (2011). In the aforementioned work, instability was suggested as the formation mechanism of the elephant trunks in this region of IC 1848E, our unstable radiatively driven shock driving into a pre-existing density structure supports this hypothesis.

4.1.6 Comparison with iVINE

There are some differences between the results obtained here and those of Gritschneder et al. (2009), the work on which our model parameters are based. In particular the maximum density evolutions derived by TORUS are much weaker, to the extent that no clear gravitational collapse has occurred by 200 kyr. This discrepancy is attributed to the difference in grid size, combined with the use of periodic boundary conditions. A significant proportion of the compression of the BES in the iVINE models arises because hot gas is advected off the edge of the periodic boundary and impacts the cloud on the opposite side of the grid (see section 4.1.2 of Gritschneder et al. 2009). This effect is justified by the authors as they assume that the molecular cloud completely surrounds the triggering star, however the effect will still give rise to differences in the results obtained by our models and theirs since motion of the hot gas has longer to decay over our larger grid and is also impeded by the elephant trunks that have formed in the wings of our models. In our models, lateral compression of the BES due to motion in the hot gas through the boundaries has negligible effect and as such the BES can be considered to be isolated.

With regard to the effect of the diffuse field, a comparison with the results found using iVINE/DiVINE (Ercolano & Gritschneder 2011b) is not straightforward as the systems being modelled are very different. However we broadly agree that treating the diffuse field can lead to higher density resulting structures, particularly in our medium flux model (section 4.1.4). In our low flux model (section 4.1.5), where elephant trunks of a similar form to those created in the iVINE/DiVINE models arise, we also find that inclusion of the diffuse field increases the density and decreases the number of elephant trunks that form. We also agree that these trunks are narrowed, sometimes to the extent that the head of the trunk can become completely detached.

5 CONCLUSIONS

It is clear that a direct treatment of the diffuse field has a significant impact upon the evolution of radiation hydrodynamics calculations on parsec scales. Not only is the effectiveness of RDI sensitive to the way in which the radiation field is treated, the formation and evolution of elephant trunk structures via instability also varies.

At low and intermediate flux regimes inclusion of the diffuse field results in more efficient RDI, with both more widespread accumulation of material and, particularly in the medium flux case, a higher final maximum density. In the high flux regime however, the material around the BES

is ionized so rapidly in the diffuse and polychromatic OTS models that only a weak shock forms and RDI does not occur effectively. Generally, it is found that the extent to which RDI occurs depends strongly on the strength of the shock that is accumulated prior to driving into the BES. Regardless of the ionizing flux, if only a weak driving shock has formed collapse will occur slowly. When sufficient material is accumulated a photo-evaporative flow is found to occur before the driving shock is braked, reinforcing the shock with the resulting rocket motion. This occurs in short, sharp, bursts with the reason for this episodic behaviour hypothesised as being due to the refilling time for material in the dense shell. The high velocity ejecta carve out material around the head of the cometary structure resulting in a low density disrupted bubble. This rocket motion has a significant effect on the collapse of the BES: with the inclusion of the diffuse field, it can accur across a large part of the otherwise shadowed region and significantly narrow the resulting cometary structure.

Elephant trunks that arise due to thin shell instability are harder to form in the presence of the diffuse field as the dimples that seed them are smoothed out, and those that do form are then subject to the expected combination of thermal compression and diffuse field photoionizing radiation. Despite this the formation of elephant trunks, as the result of instability in a radiatively driven shock, still occurs and provides a mechanism for the formation of systems such as that discussed in Chauhan et al. (2011).

The radiation-hydrodynamical effect of the diffuse field is cumulative and significant, and is strongly coupled to the hydrodynamical evolution of the system. This implies that the treatment of the diffuse field should be accurate throughout a simulation, as consistent deficiencies could lead to a systematic change in the overall radiation hydrodynamical evolution of the system.

We next intend to compute synthetic images to determine theoretical observables for systems undergoing star formation as a result of radiative feedback. We will also include the use of an adaptive mesh so that we can follow collapse until the onset of star formation.

6 SUMMARY

We have used the radiation hydrodynamics module of the TORUS code to investigate the effects of using a monochromatic OTS, polychromatic OTS and polychromatic-diffuse field on the radiatively driven implosion of a Bonnor-Ebert sphere. We have found that incorporating the diffuse field into this model over three flux regimes leads to significantly different results to those obtained using the OTS approximation. At intermediate and low flux regimes the rate of compression is higher than that without inclusion of the diffuse field, whereas at high flux compression actually occurs more slowly when the diffuse or polychromatic OTS field is considered because there is little opportunity for a material shock to drive into the BES. In the event of accumulation of sufficient material, photo-evaporative flow or ejection has been identified as a mechanism which can drive collapse very effectively. This photo-evaporative flow is particularly effective at driving and compressing the tail of the cometary

structure when the diffuse field is treated. The formation of elephant trunk structures via instability also occurs much less readily with the inclusion of the diffuse field as perturbations to the ionization front are smeared out. We conclude that in order to properly address quantitative questions regarding triggered star formation thorough treatment of the diffuse field is necessary in radiation hydrodynamics models.

REFERENCES

Acreman D. M., Douglas K. A., Dobbs C. L., Brunt C. M., 2010, MNRAS, 406, 1460

Agertz O., Moore B., Stadel J., Potter D., Miniati F., Read J., Mayer L., Gawryszczak A., Kravtsov A., Nordlund Å., Pearce F., Quilis V., Rudd D., Springel V., Stone J., Tasker E., Teyssier R., Wadsley J., Walder R., 2007, MNRAS, 380, 963

Arthur S. J., Hoare M. G., 2006, ApJS, 165, 283

Bertoldi F., 1989, ApJ, 346, 735

Bertoldi F., McKee C. F., 1990, ApJ, 354, 529

Bisbas T. G., Wünsch R., Whitworth A. P., Hubber D. A., 2009, A&A, 497, 649

Bisbas T. G., Wünsch R., Whitworth A. P., Hubber D. A., Walch S., 2011, ApJ, 736, 142

Chauhan N., Ogura K., Pandey A. K., Samal M. R., Bhatt B. C., 2011, PASJ, 63, 795

Dale J. E., Bonnell I. A., Whitworth A. P., 2007, MNRAS, 375, 1291

Elmegreen B. G., 2011, ArXiv e-prints

Elmegreen B. G., Kimura T., Tosa M., 1995, ApJ, 451, 675

Elmegreen B. G., Lada C. J., 1977, ApJ, 214, 725

Ercolano B., Barlow M. J., Storey P. J., Liu X., 2003, MNRAS, 340, 1136

Ercolano B., Gritschneder M., 2011a, in J. Alves, B. G. Elmegreen, J. M. Girart, & V. Trimble ed., Computational Star Formation Vol. 270 of IAU Symposium, Ionisation Feedback in Star and Cluster Formation Simulations. pp 301–308

Ercolano B., Gritschneder M., 2011b, MNRAS, 413, 401

Ferland G., 1995, in R. Williams & M. Livio ed., The Analysis of Emission Lines: A Meeting in Honor of the 70th Birthdays of D. E. Osterbrock and M. J. Seaton The Lexington Benchmarks for Numerical Simulations of Nebulae. pp 83–+

Ferland G. J., Korista K. T., Verner D. A., Ferguson J. W., Kingdon J. B., Verner E. M., 1998, PASP, 110, 761

Garcia-Segura G., Franco J., 1996, ApJ, 469, 171

Gritschneder M., Burkert A., Naab T., Walch S., 2010, ApJ, 723, 971

Gritschneder M., Naab T., Burkert A., Walch S., Heitsch F., Wetzstein M., 2009, MNRAS, 393, 21

Gritschneder M., Naab T., Walch S., Burkert A., Heitsch F., 2009, ApJ, 694, L26

Harries T. J., 2000, MNRAS, 315, 722

Harries T. J., 2011, MNRAS, 416, 1500

Harries T. J., Howarth I. D., 1997, A&AS, 121, 15

Harries T. J., Monnier J. D., Symington N. H., Kurosawa R., 2004, MNRAS, 350, 565

Hartmann L., 2009, Accretion Processes in Star Formation: Second Edition. Cambridge University Press

Henney W. J., Arthur S. J., de Colle F., Mellema G., 2009, MNRAS, 398, 157

Herbig G. H., 1962, ApJ, 135, 736

Kelvin W. T., 1871, Philosophical Magazine, 42, 362

Kessel-Deynet O., Burkert A., 2003, MNRAS, 338, 545

Kurosawa R., Harries T. J., Bate M. R., Symington N. H., 2004, MNRAS, 351, 1134

Lada C. J., Lada E. A., 2003, ARA&A, 41, 57

Lucy L. B., 1999, A&A, 344, 282

Mellema G., Iliev I. T., Alvarez M. A., Shapiro P. R., 2006, 11, 374

Mizuta A., Kane J. O., Pound M. W., Remington B. A., Ryutov D. D., Takabe H., 2006, ApJ, 647, 1151

Ogura K., Sugitani K., Pickles A., 2002, AJ, 123, 2597

Oort J. H., Spitzer Jr. L., 1955, ApJ, 121, 6

Osterbrock D. E., 1989, Astrophysics of gaseous nebulae and active galactic nuclei

Peters T., Banerjee R., Klessen R. S., 2008, Physica Scripta Volume T, 132, 014026

Preibisch T., Zinnecker H., 2007, in B. G. Elmegreen & J. Palous ed., IAU Symposium Vol. 237 of IAU Symposium, Sequentially triggered star formation in OB associations. pp 270–277

Price D. J., 2008, Journal of Computational Physics, 227, 10040

Rayleigh L., 1900, Proceedings of the London mathematical society, 14, 170

Reach W. T., Rho J., Young E., Muzerolle J., Fajardo-Acosta S., Hartmann L., Sicilia-Aguilar A., Allen L., Carey S., Cuillandre J.-C., Jarrett T. H., Lowrance P., Marston A., Noriega-Crespo A., Hurt R. L., 2004, ApJS, 154, 385

Rhie C. M., Chow W. L., 1983, AIAA Journal, 21, 1525

Roe P. L., 1985, in R. L. Lee, R. L. Sani, T. M. Shih, & P. M. Gresho ed., Large-Scale Computations in Fluid Mechanics Some contributions to the modelling of discontinuous flows. pp 163–193

Schneps M. H., Ho P. T. P., Barrett A. H., 1980, ApJ, 240, 84

Sedov L. I., 1946, Journal of applied mathematics and mechanics, 10, 241

Sod G. A., 1978, J. Comput. Phys., 27, 1

Spitzer L., 1978, Physical processes in the interstellar medium

Taylor G., 1950a, Proc. R. Soc., 201, 192

Taylor G., 1950b, Royal Society of London Proceedings Series A, 201, 159

Vishniac E. T., 1983, ApJ, 274, 152

Von Helmholtz H., 1868, Monthly Reports of the Royal Prussian Academy of Philosophy in Berlin, 23, 215

Williams R. J. R., 2002, MNRAS, 331, 693

Wood K., Mathis J. S., Ercolano B., 2004, MNRAS, 348, 1337

Zavagno A., Deharveng L., Comerón F., Brand J., Massi F., Caplan J., Russeil D., 2006, A&A, 446, 171